



Predicted Sensitivity of Neutrino Oscillation Tomography to the Properties of Large Low-Velocity Provinces in the Lower Mantle

Authors: **Yael Deniz**¹, Eric Mittelstaedt¹, Joao Coelho², Veronique VanElewyck^{2,3}, Isabel Goos^{2,4}, Stephanie Durand⁵, Nobuaki Fuji^{3,4}.

¹University of Idaho, Department of Earth and Spatial Sciences, Moscow, ID, United States

²Université Paris Cité, CNRS, Astroparticule et Cosmologie

³Institut Universitaire de France

⁴Université Paris Cité, Institut de Physique du Globe de Paris, CNRS

⁵Laboratoire de Géologie de Lyon: Terre, Planètes, Environnement, CNRS, UMR 5276, École Normale Supérieure de Lyon, Université de Lyon, Université Claude Bernard Lyon



EAR-2406115

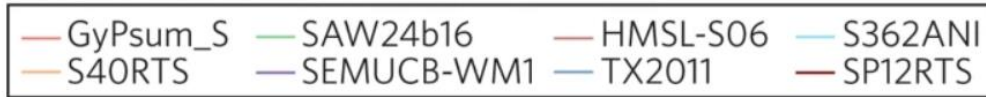
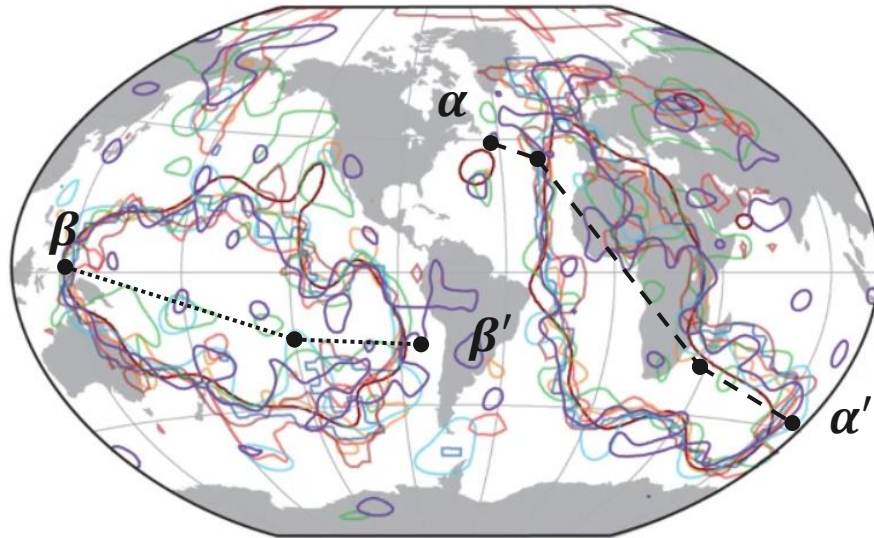
October 29, 2025



Seismic data reveals two Large Low Velocity Provinces (LLVPs) a top of the Core-Mantle-Boundary(CMB)

Morphology of LLVPs

Vote map of different shear wave velocity (V_S) data sets

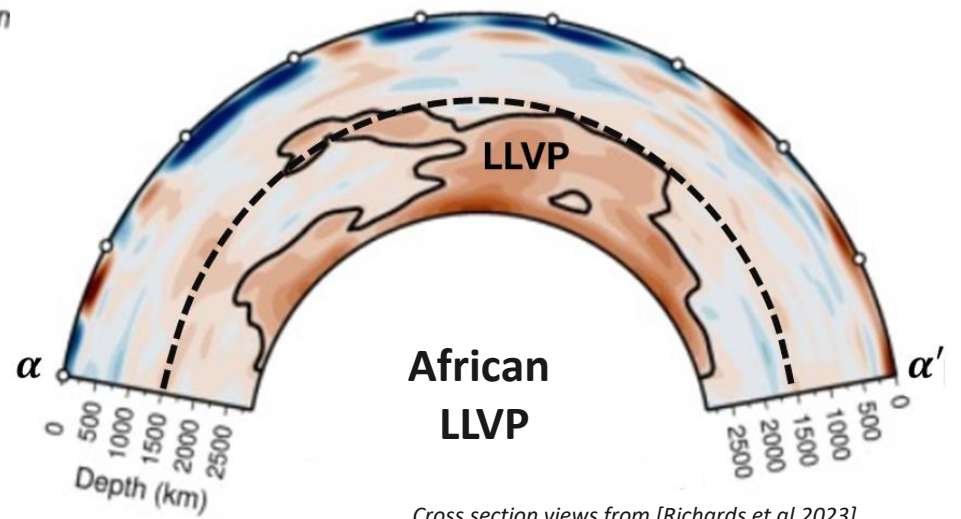
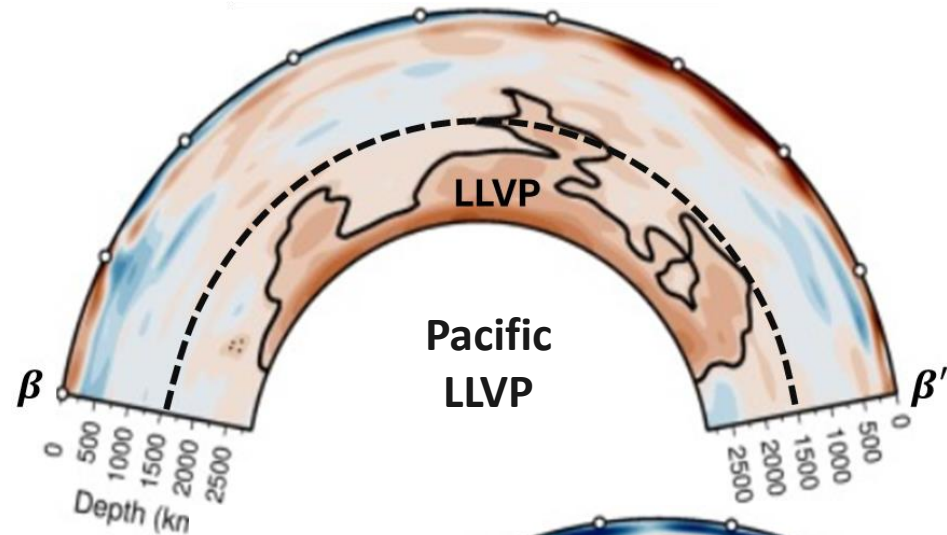


Vote map modified from [Lekic et al., 2012; Garnero et al., 2016]

LLVPs cover ~30% of the Core-Mantle-Boundary (CMB) surface, extending $\sim 10^3$ km laterally and vertically [Davies et al., 2015; McNamara et al., 2019, Richards et al,2023]

LLVP cross-section view

Along the $\beta\beta'$ ($\alpha\alpha'$) line



Cross section views from [Richards et al,2023]



Current estimates of LLVP matter properties are uncertain. Different constraints sometimes produce contradictory results

ARTICLE

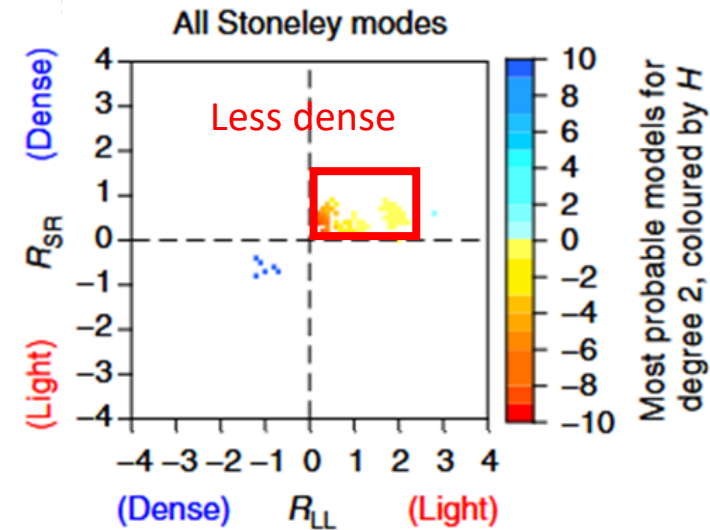
Received 18 Aug 2015 | Accepted 13 Mar 2017 | Published 15 May 2017

DOI: 10.1038/ncomms15241 OPEN

Density structure of Earth's lowermost mantle from Stoneley mode splitting observations

Paula Koelemeijer^{1,2}, Arwen Deuss³ & Jeroen Ritsema⁴

Most-probable models have **overall less dense LLVPs** relative to surroundings ($\sim -0.88\%$)



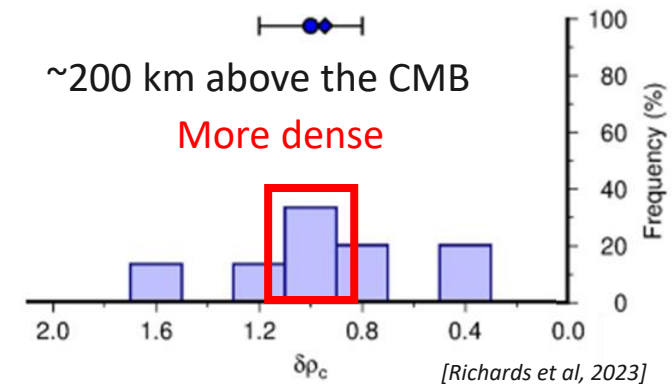
Modified from [Koelemeijer et al, 2017]

Geodynamic, geodetic, and seismic constraints favour deflated and dense-cored LLVPs

Fred D. Richards^{a,*}, Mark J. Hoggard^b, Sia Ghelichkhan^b, Paula Koelemeijer^{c,d}, Harriet C.P. Lau^{e,f}

Accepted 9 December 2022

Bottom $\sim 100\text{--}200$ km of LLVPs is **more dense**



[Richards et al, 2023]



Current estimates of LLVP matter properties are uncertain. Different constraints sometimes produce contradictory results

ARTICLE

Received 18 Aug 2015 | Accepted 13 Mar 2017 | Published 15 May 2017

DOI: 10.1038/ncomms15241 OPEN

Density structure of Earth's lowermost mantle from Stoneley mode splitting observations

Paul **ARTICLE**

doi:10.1038/nature24452

Tidal tomography constrains Earth's deep-mantle buoyancy

Harriet C. P. Lau¹, Jerry X. Mitrovica¹, James L. Davis², Jeroen Tromp³, Hsin-Ying Yang^{4,5} & David Al-Attar⁶

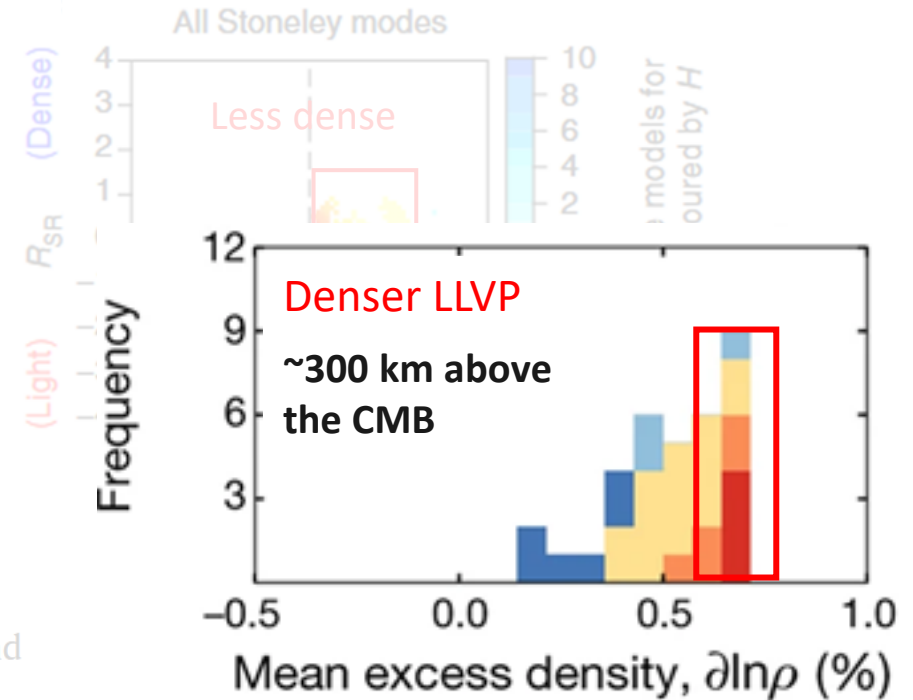
Article | Published: 16 November 2017

The bottom ~2/3 of the LLSVPs are about 0.5–0.6% denser than average mantle

Fred D. Richards^{a,*}, Mark J. Hoggard^b, Sia Ghelichkhan^b, Paula Koelemeijer^{c,d}, Harriet C.P. Lau^{e,f}

Accepted 9 December 2022

Bottom ~100–200 km of LLVPs is more dense



Modified from [Lau et al, 2017]

[Richards et al, 2023]



Current estimates of LLVP matter properties are uncertain. Different constraints sometimes produce contradictory results

Constraints on the composition and temperature of LLSVPs from seismic properties of lower mantle minerals

Kenny Vilella^{a,b,*}, Thomas Bodin^c, Charles-Edouard Boukaré^d, Frédéric Deschamps^b, James Badro^e, Maxim D. Ballmer^{g,f}, Yang Li^h

Bridgmanite (*Bm*)

[MgSiO₃/ FeSiO₃/ FeAlO₃
Al₂O₃/ Fe₂O₃]

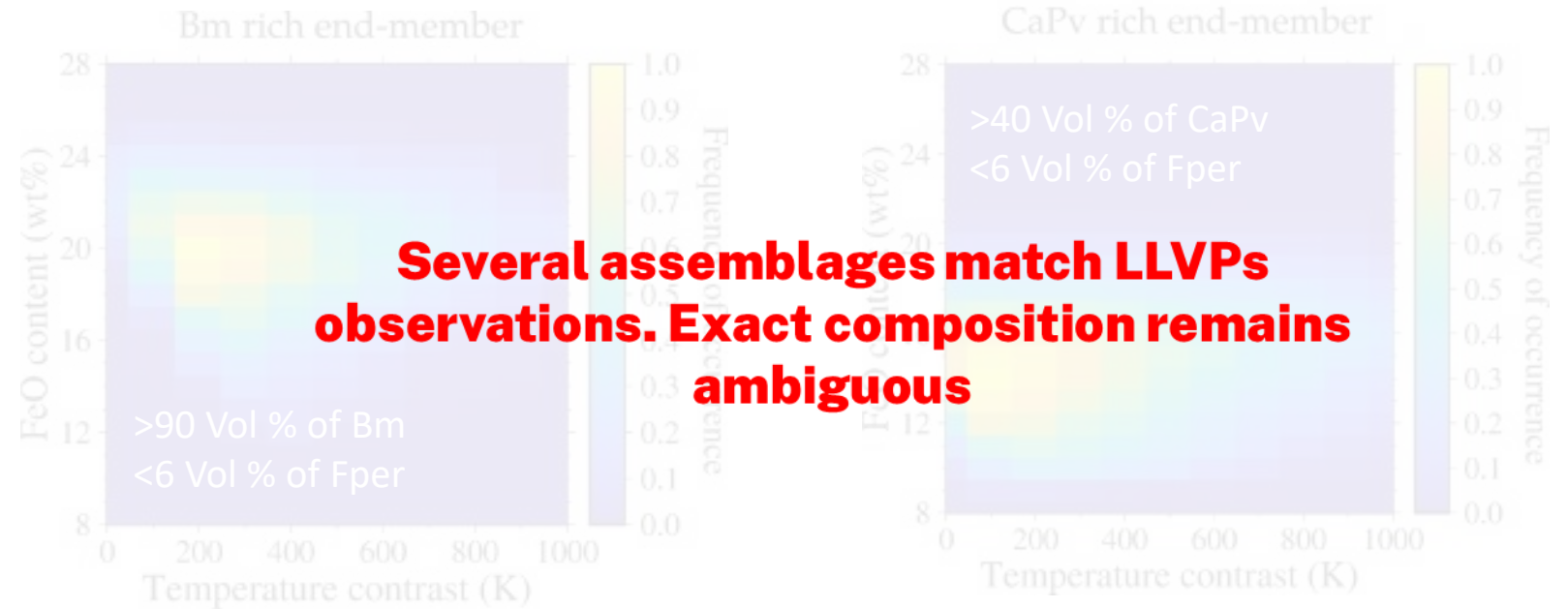
Ca-Perovskite (*CaPv*)

[CaSiO₃]

Ferropericlase (*Fper*)

[MgO, FeO]

79000 cases explain the seismic observations



Assemblage conditions

FeO 14 – 25 wt%

Al₂O₃ > 8 wt%

R_{Fe} > 0.6

Assemblage conditions

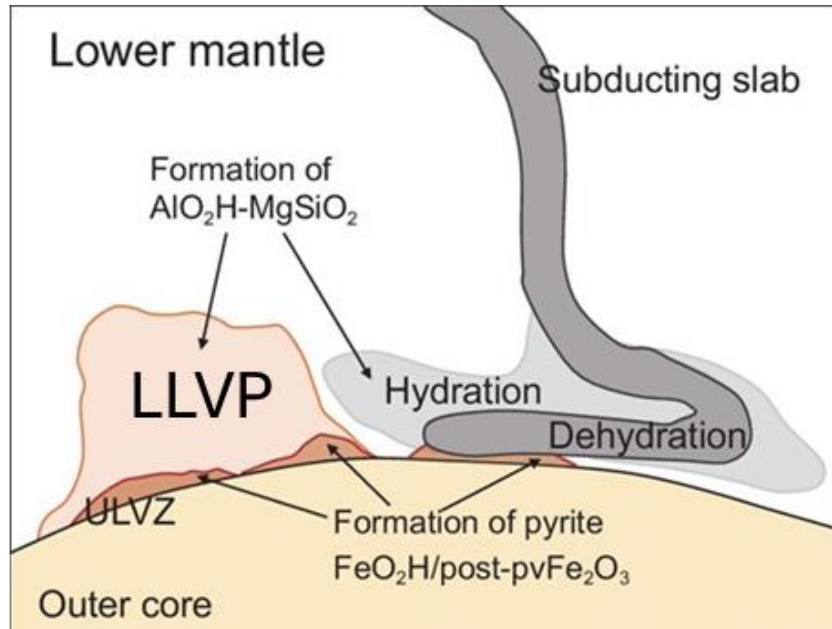
FeO 10 – 21wt%

Al₂O₃ 3 – 13 wt%

R_{Fe} > 0.3

We have no constraints on the possible presence of hydrogen in LLVPs

Presence of hydrogen in lower mantle minerals



Modified from [Othani et al, 2019]

Theoretical studies on the hydrous lower mantle and D'' layer minerals

Jiajun Jiang^{a,b}, Feiwu Zhang^{a,*}

^a State Key Laboratory of Ore Deposit Geochemistry, Institute of Geochemistry, Chinese Academy of Sciences, Guiyang 550081, China

^b University of Chinese Academy of Sciences, Beijing 100049, China

Accepted 1 August 2019

JOURNAL ARTICLE

The role of water in Earth's mantle

Eiji Ohtani

National Science Review, Volume 7, Issue 1, January 2020, Pages 224–232, [https://](https://doi.org/10.1093/nsr/nwz071)

doi.org/10.1093/nsr/nwz071

Published: 11 June 2019

Water (**Hydrogen**) inclusion in lower-mantle perovskites (e.g., Bridgmanite) **may explain LLVP seismic signal**

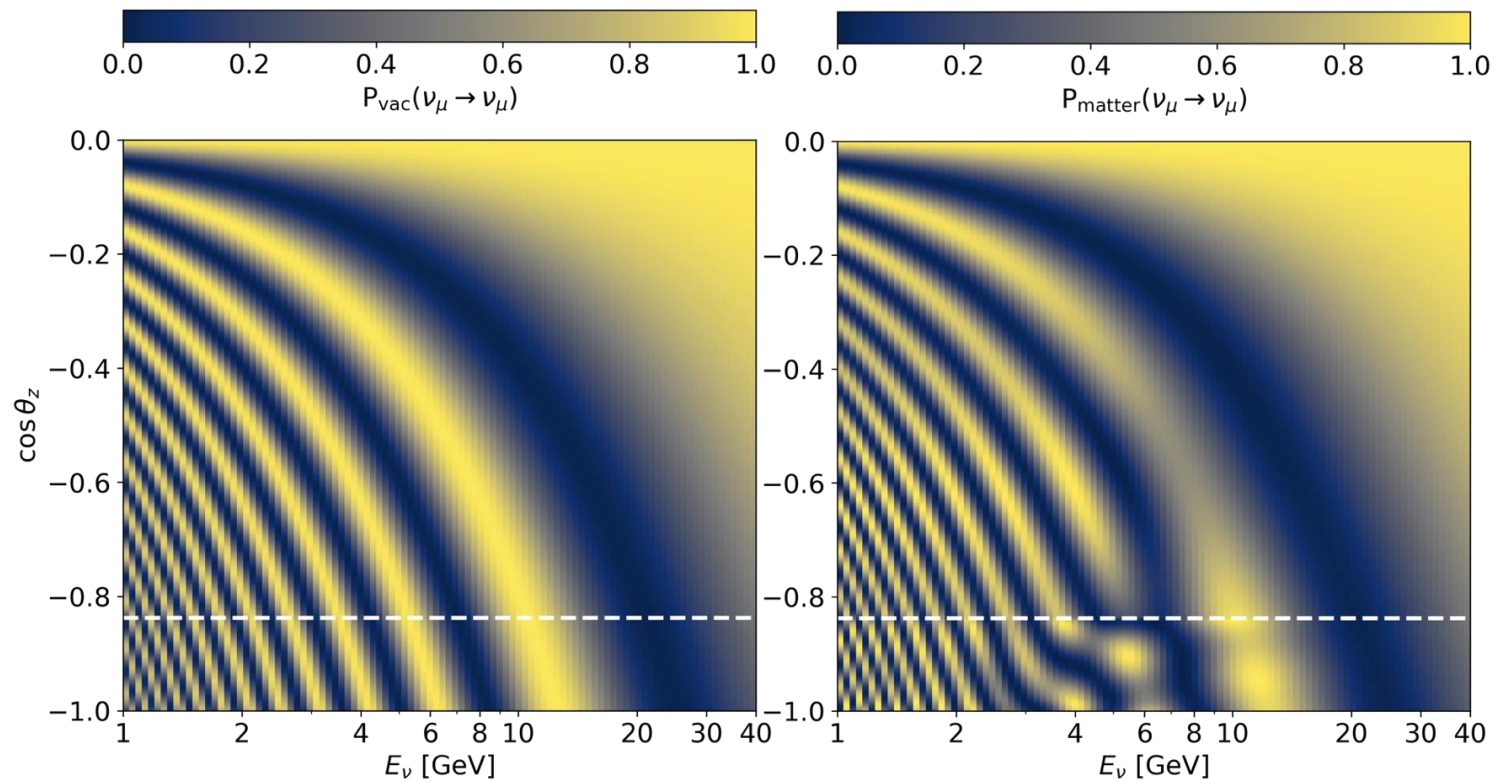
[Othani et al, 2019; Jiang & Zhang, 2019]

Constraints on lower-mantle hydrogen are scarce



Different Earth matter profiles produce different neutrino oscillation probabilities

Oscillation probability distribution for different matter profiles





Different Earth matter profiles produce different neutrino oscillation probabilities

Two-flavor approximation oscillation probability

$$P_{\nu_\alpha \rightarrow \nu_\beta}^m(L, E_\nu) = \sin^2(2\theta^m(n_e)) \sin^2\left(\frac{\Delta^m m^2(n_e)L}{4E_\nu}\right)$$

$$P_{\nu_\alpha \rightarrow \nu_\alpha}^m(L, E_\nu) = 1 - P_{\nu_\alpha \rightarrow \nu_\beta}^m(L, E_\nu)$$

Electron number density:

$$n_e = \frac{\rho Y_e N_A}{M_u}$$

N_A : Avogadro's number
 M_u : molar mass constant
 ρ : Matter density

Electron yield

(Number ratio of protons (Z) to nucleons (A)):

$$Y_e = \sum_i w_i \cdot \left(\frac{Z}{A}\right)_i$$

Different Earth matter profiles correspond to **different density** (ρ) and **electron yield** (Y_e) **profiles**, and therefore **produce different distribution patterns of neutrino oscillation probabilities**

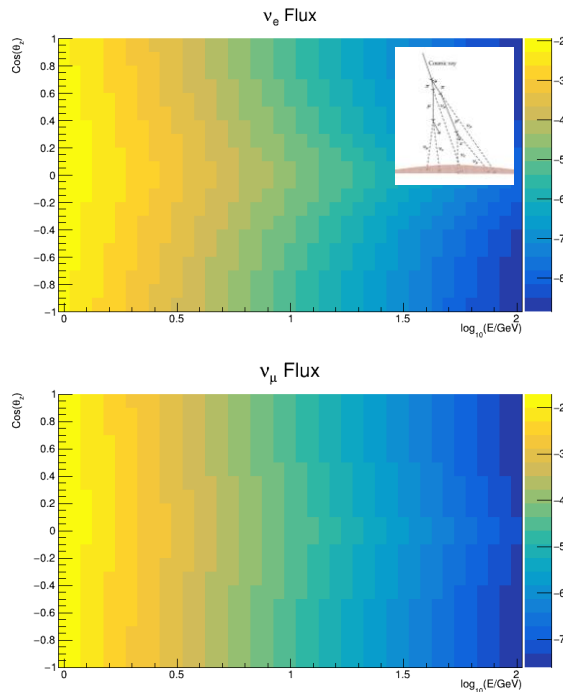
**Sum over all elements that make up the propagation medium



Oscillation tomography exploits the matter dependence of neutrino oscillation probabilities to probe Earth's interior.

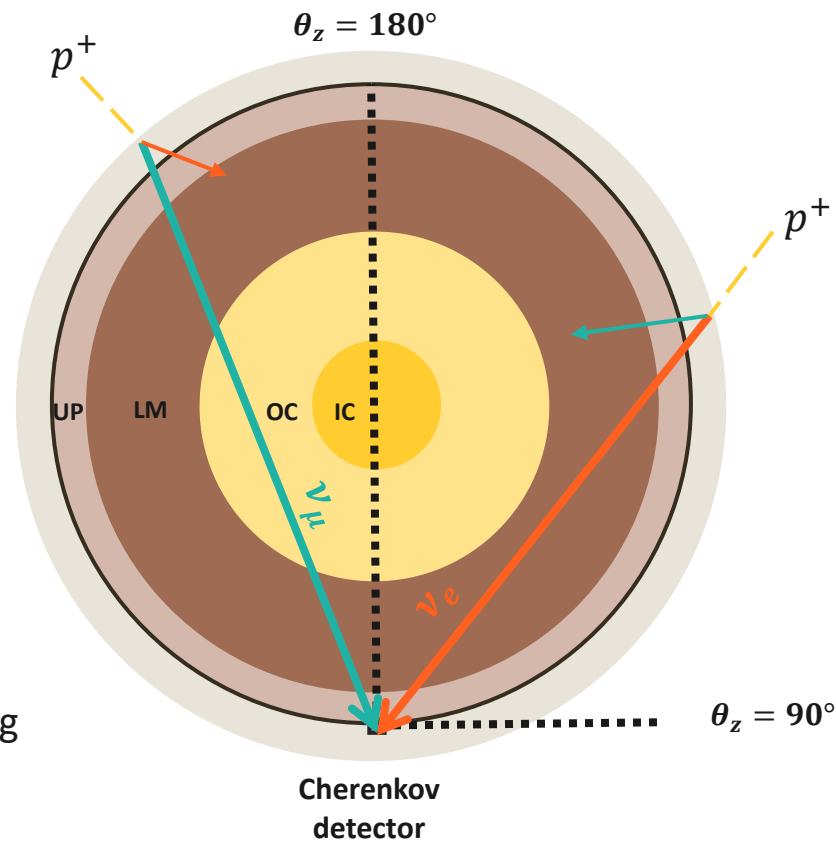
Oscillation Tomography: The Checklist

1) Neutrino Source: Atmosphere

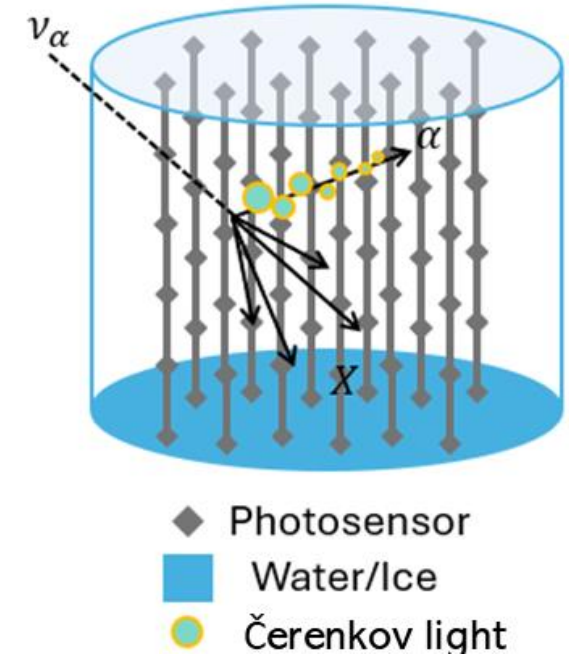


Neutrino flux obtained by interpolating the Honda flux tables [Honda et al, 2015]

2) Propagation model for the Earth



3) Neutrino detector (e.g., Cherenkov)

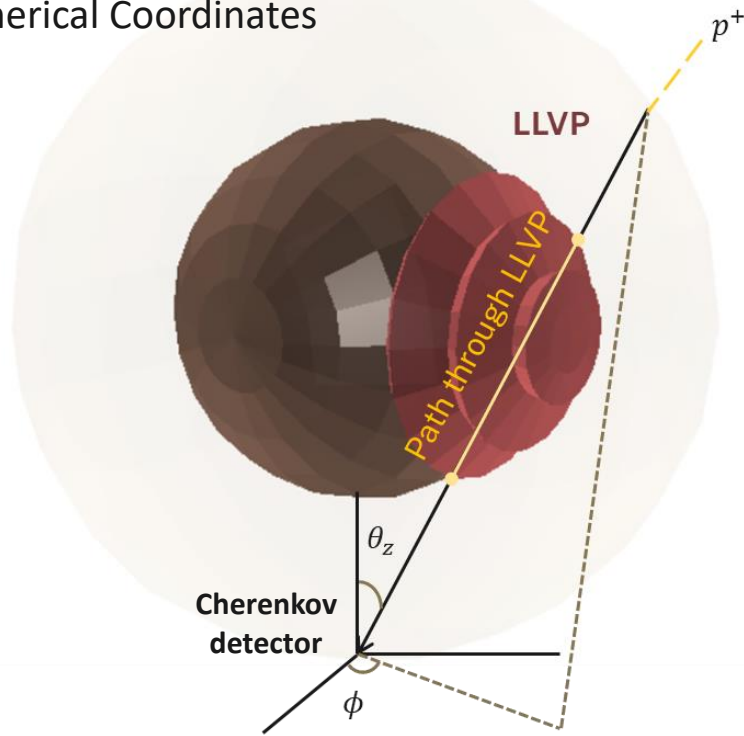




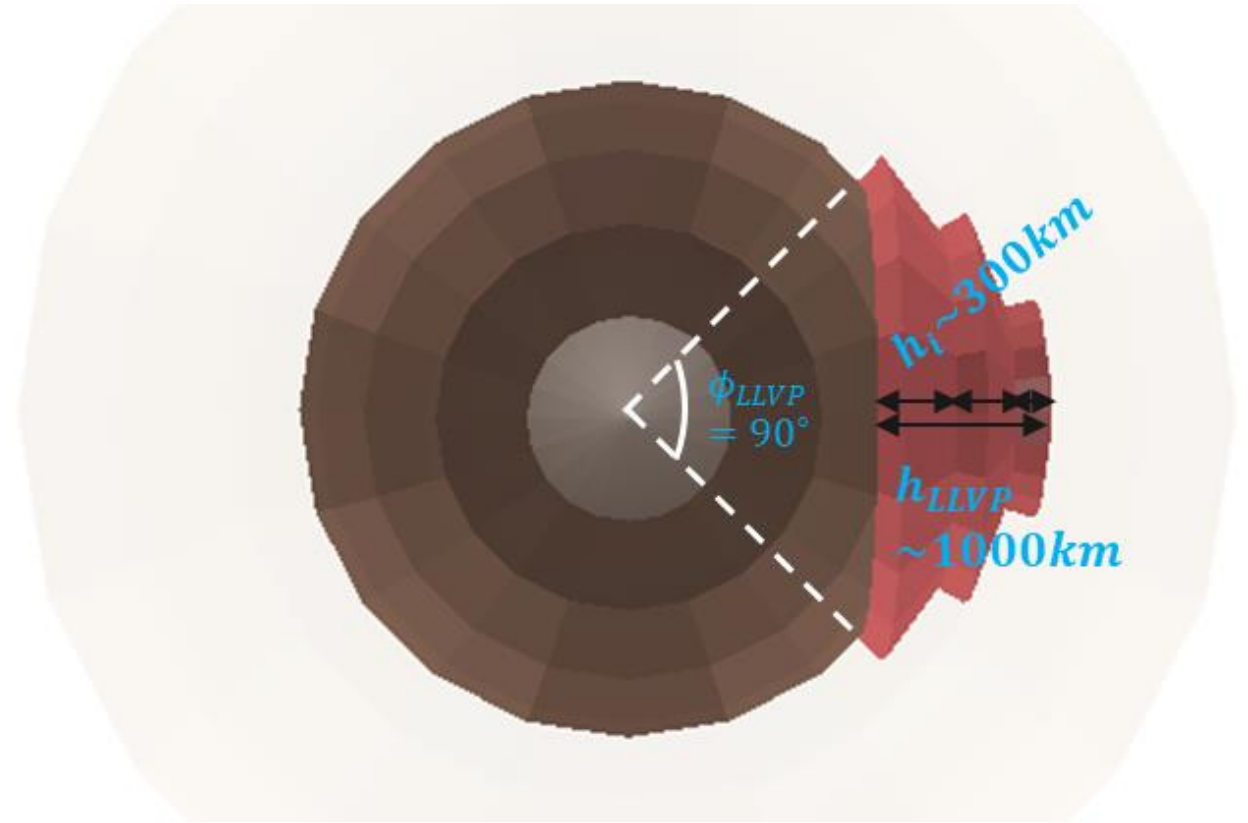
Oscillation tomography uses exploits matter Effect to probe specific regions of the Earth

The m-LLVP: a simplified geometric model that approximates the true, complex shape of LLVPs

Detector-Centered
Spherical Coordinates



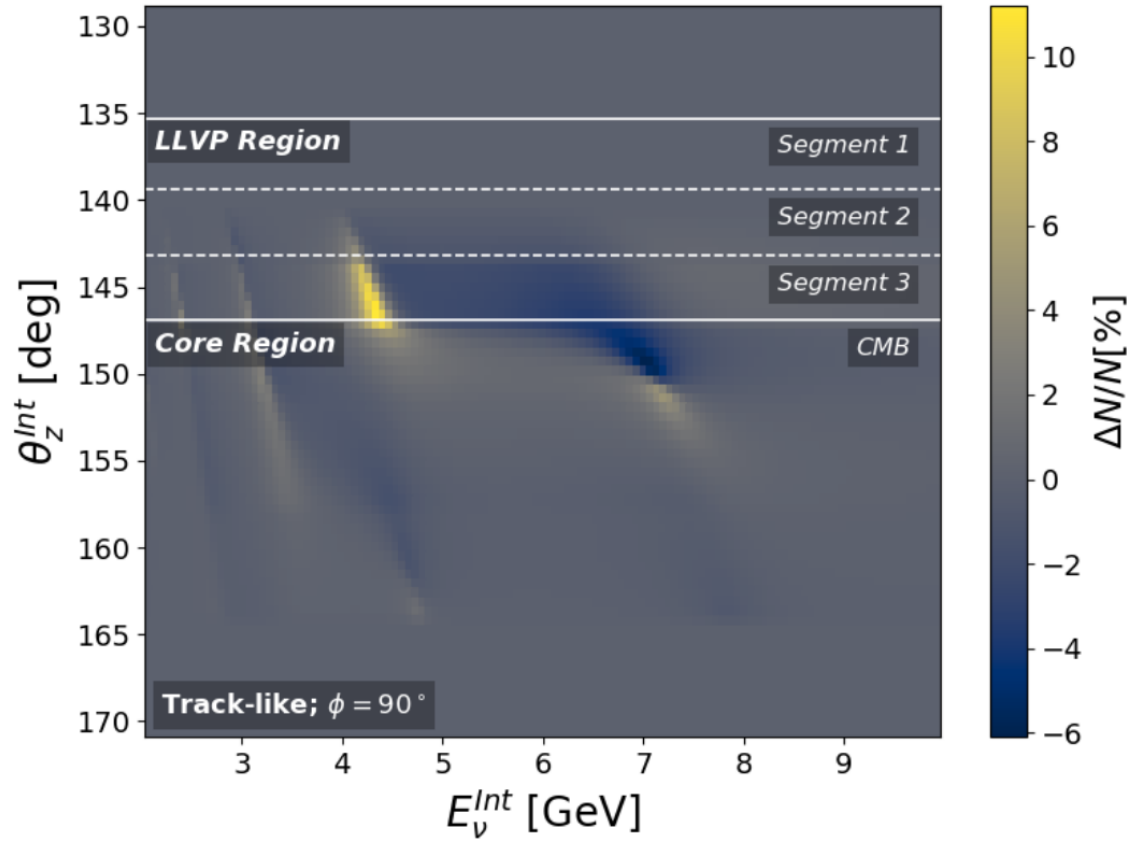
For simplicity, the detector location is chosen to be the South Pole.



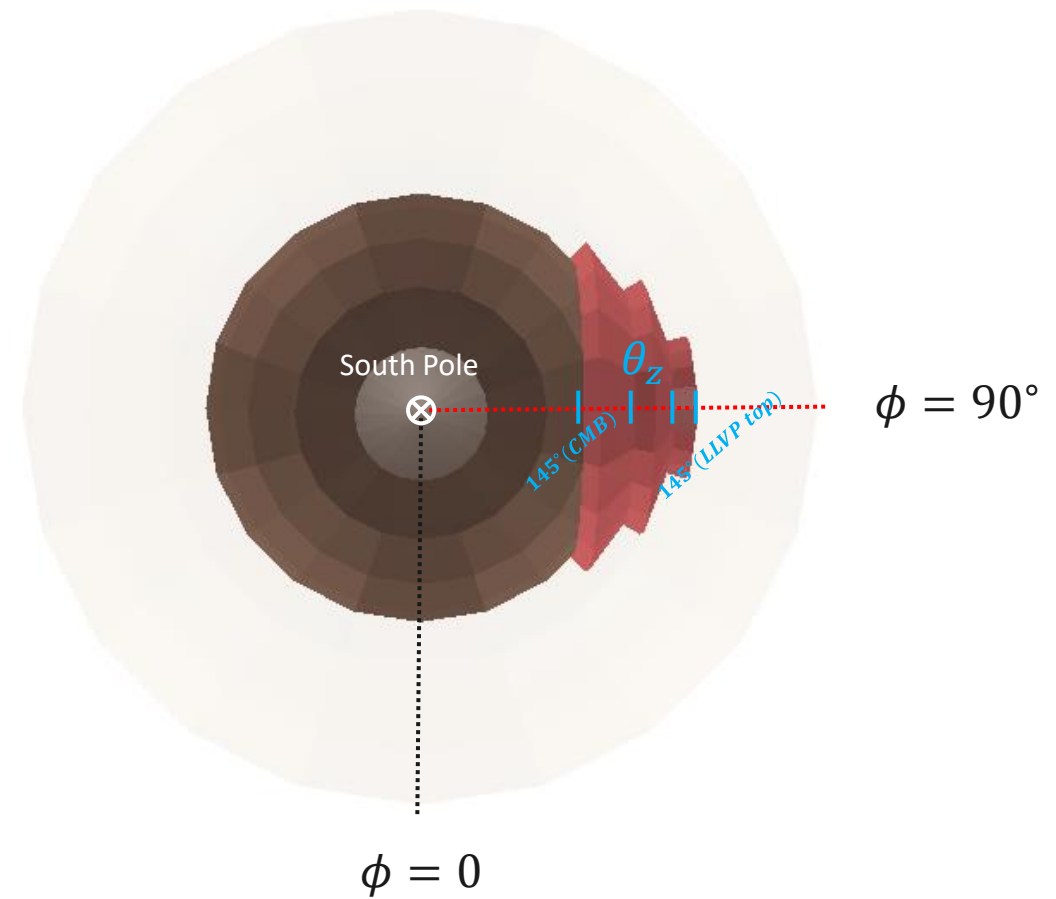
the South Pole view

The Presence of the m-LLVP modifies the distribution of neutrino events

Ideal detector



Visualization of neutrino directions in model

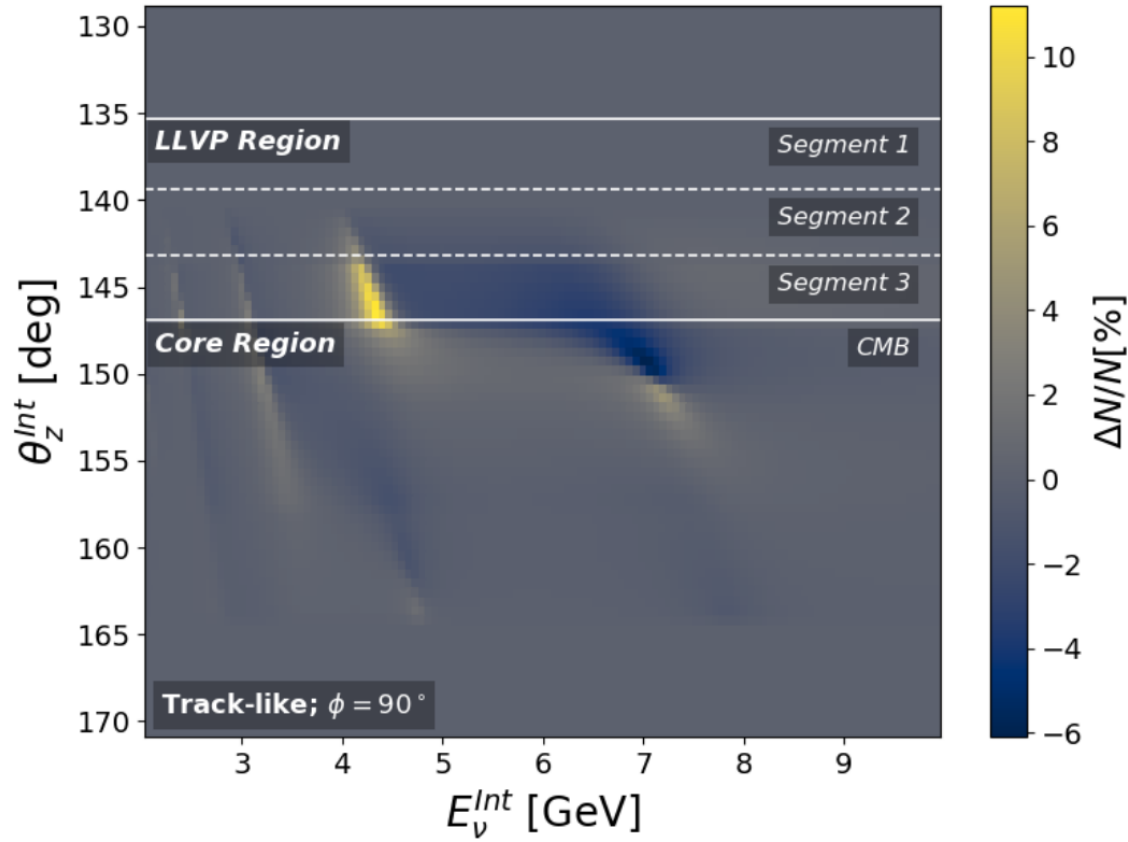




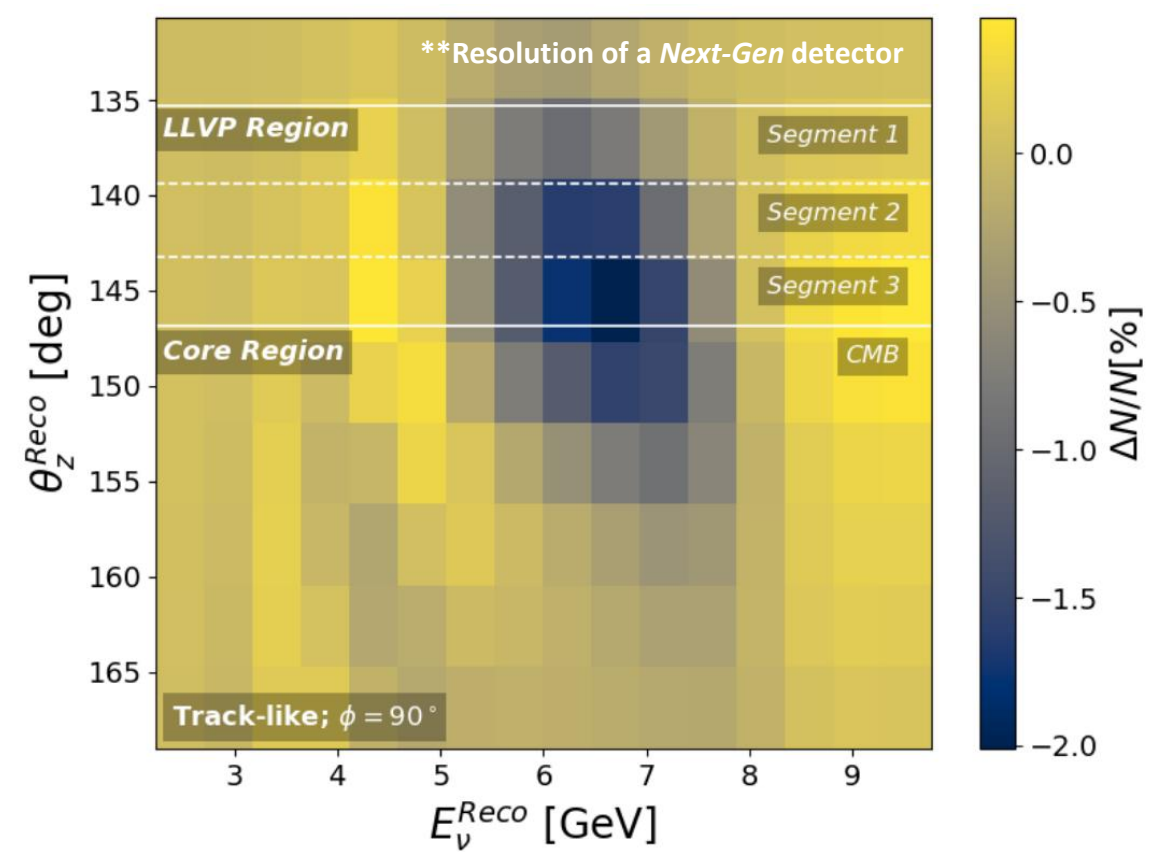
The Presence of the m-LLVP modifies the distribution of neutrino events

To generate a **realistic** event **distribution**, we must include detector **resolution** effects

Ideal detector



Realistic detector

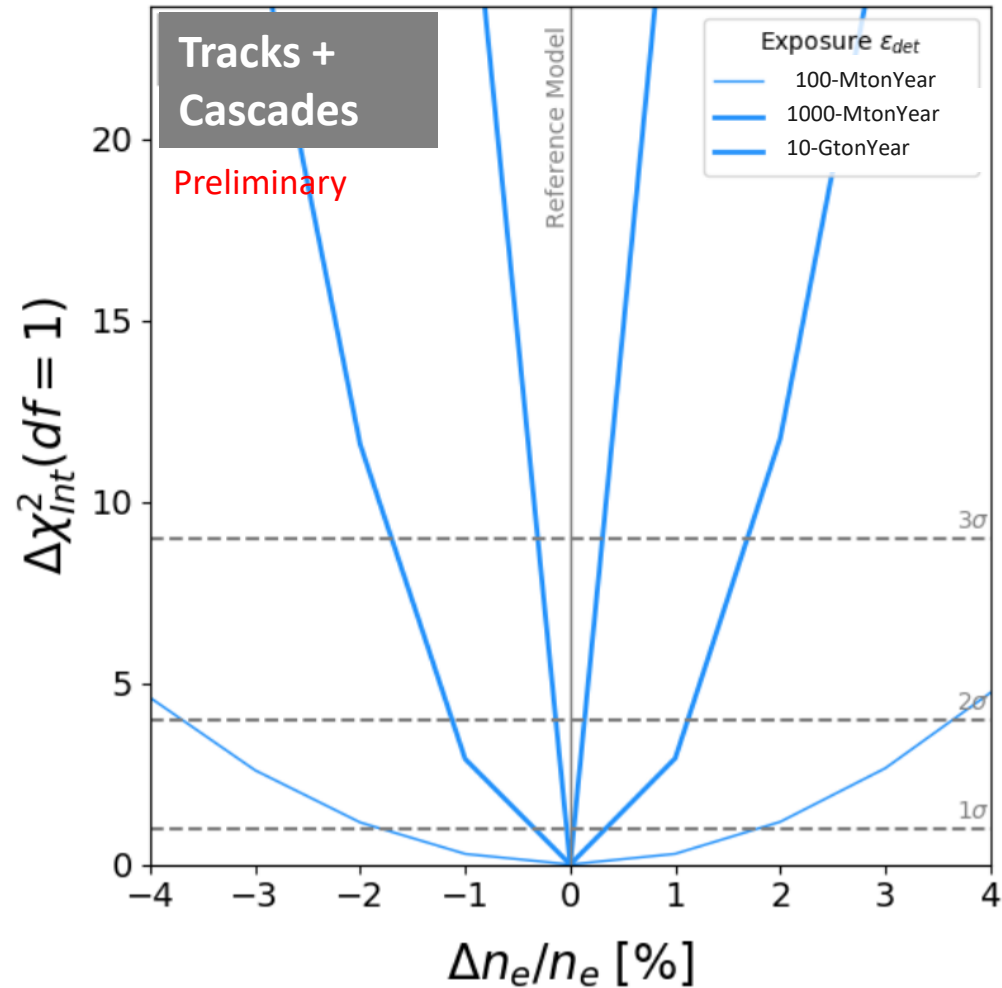




LLVPs are resolvable by neutrino detectors

The $\Delta\chi(1)^2$ test between n_{exp} (PREM) and n_{obs} (m-LLVP) gives sensitivity

Perfect resolution

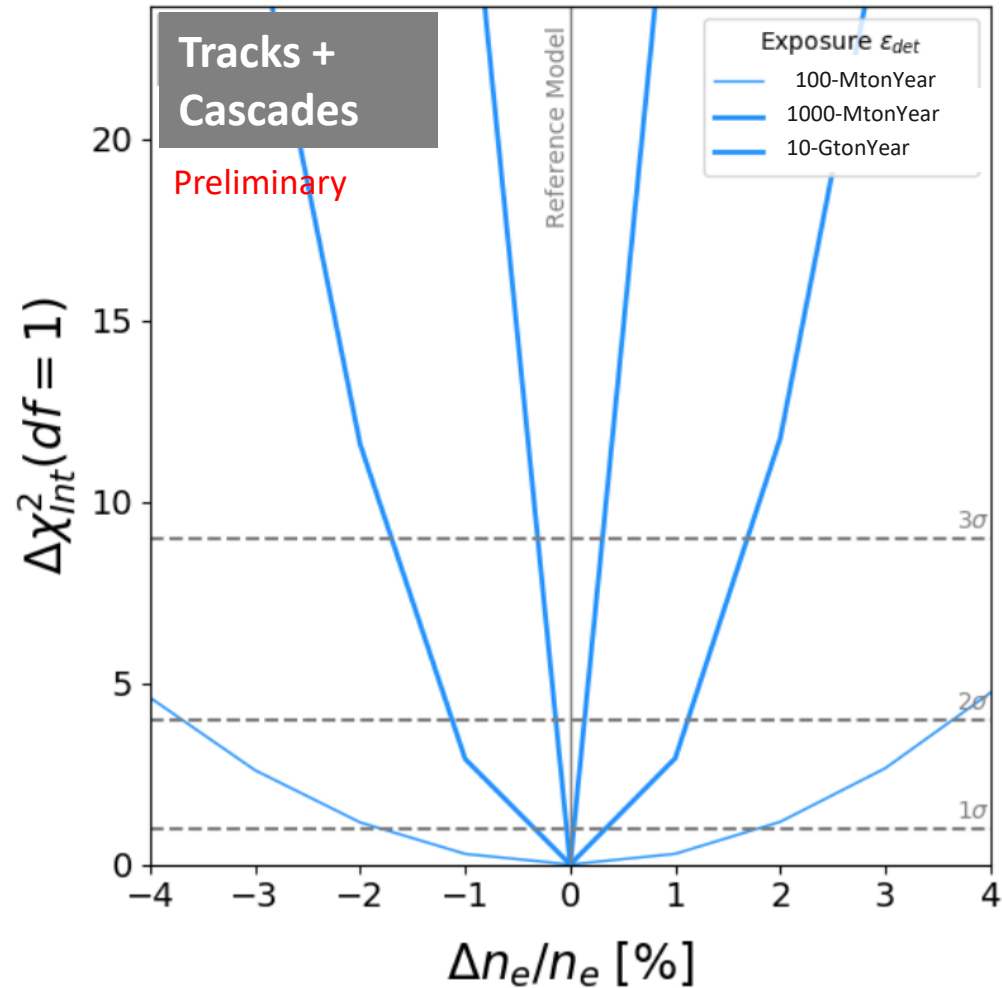




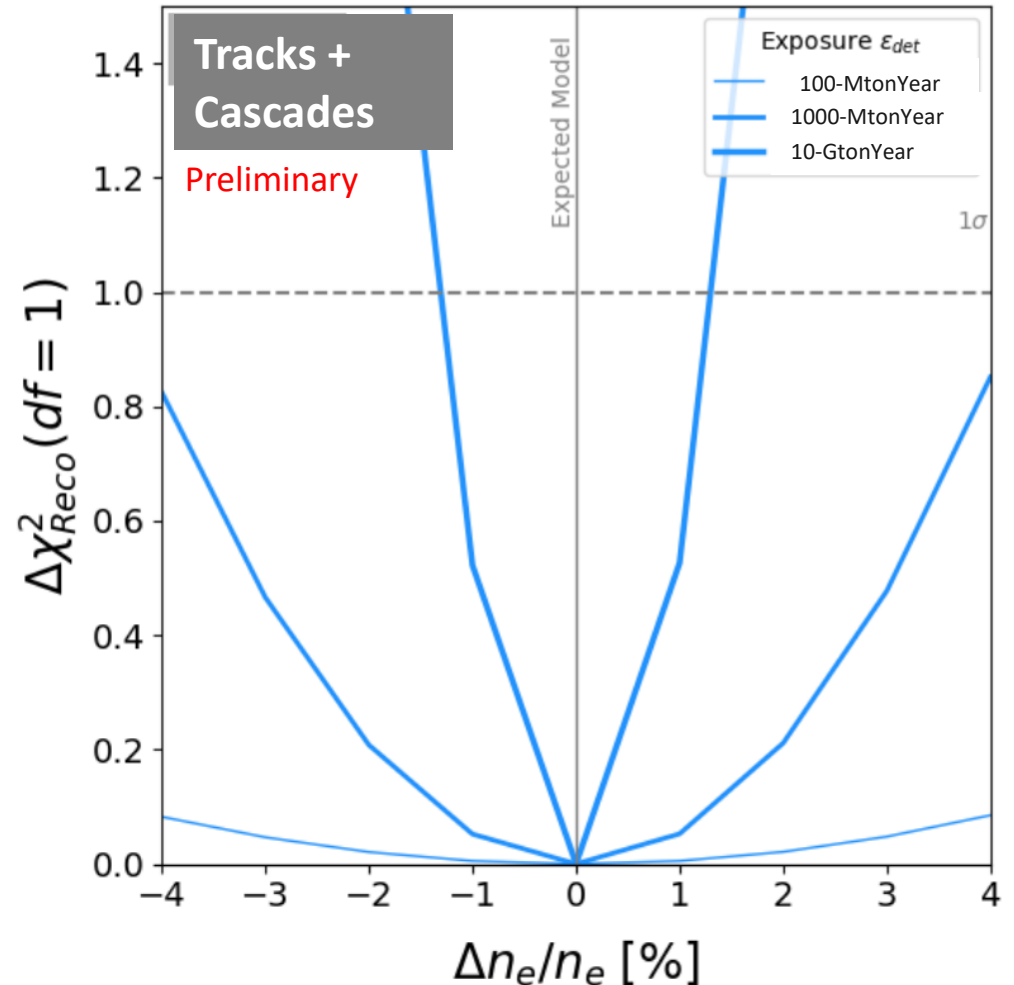
LLVPs are resolvable by neutrino detectors

The $\Delta\chi(1)^2$ test between n_{exp} (PREM) and n_{obs} (m-LLVP) gives sensitivity

Perfect resolution



Realistic resolution





Using Vilella et al.'s end-member composition, we choose assemblages that meet the stated bulk conditions

Phases in the LLVP assemblage

Bridgmanite (**Bm**)

MgSiO₃ / FeSiO₃ / FeAlO₃ / Al₂O₃ / Fe₂O₃

Reference mol % 89.6/ 3.7/ 3.7/ 3/ 0

Reference vol % 75

Ca-Perovskite (**CaPv**)

CaSiO₃

Reference vol % 7

Ferropericlase (**Fper**)

MgO / FeO

Reference mol % 81.4/ 0.186

Reference vol % 18

Reference Bulk

Properties

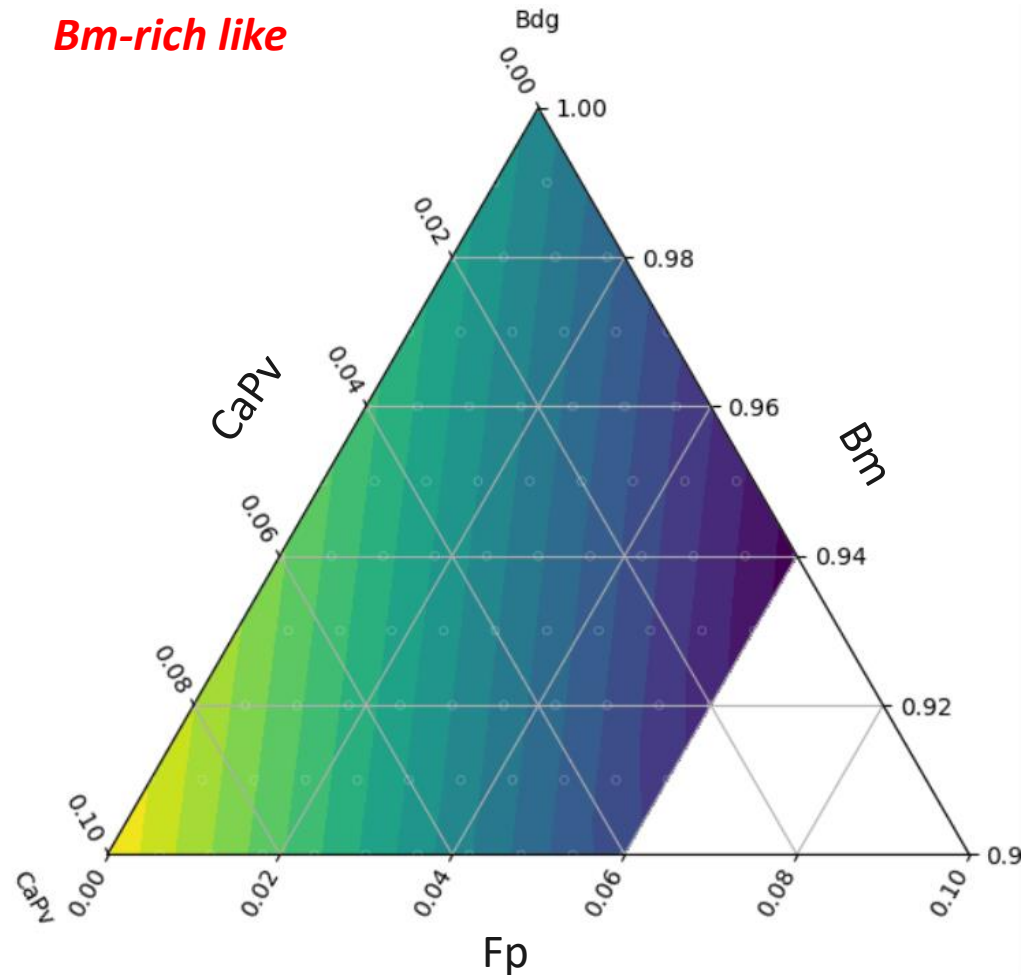
FeO ~ 8 wt%

Al₂O₃ ~ 3.6 wt%

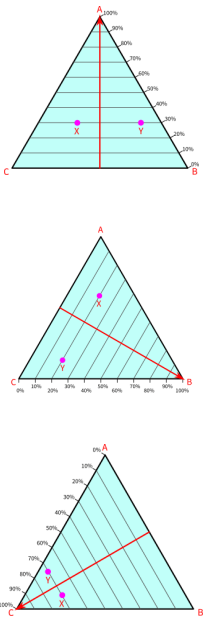
R_{Fe} ~ 0.5

Density contrast for different assemblages

Bm-rich like



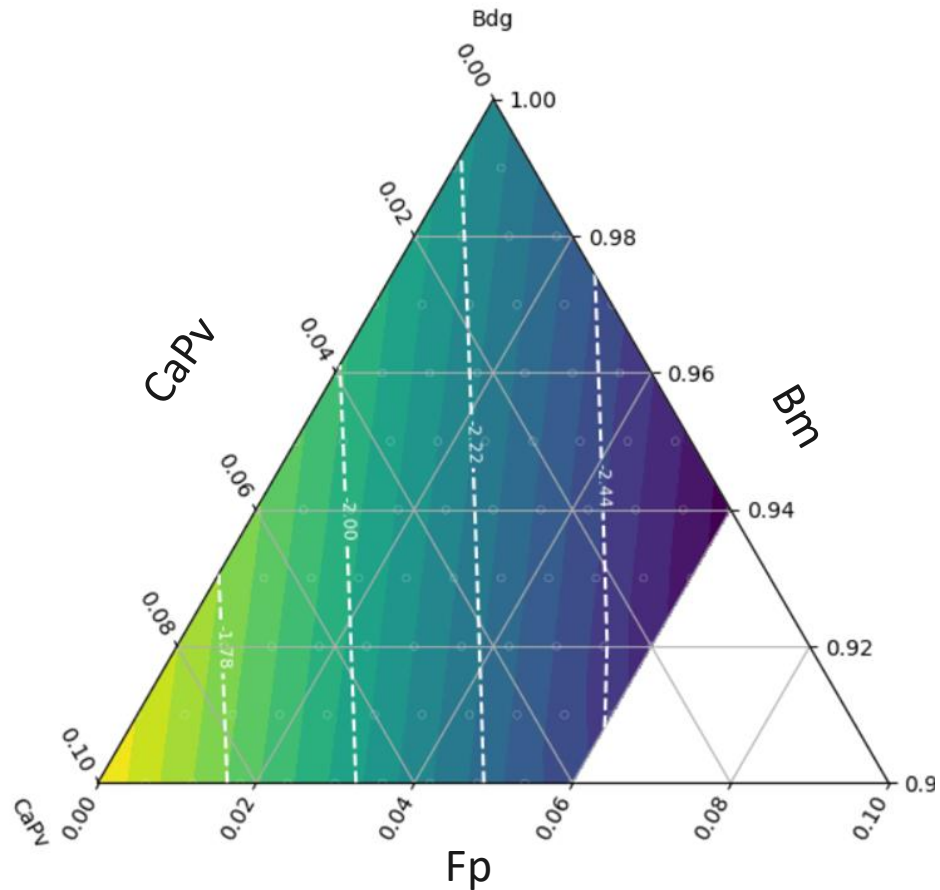
How to read



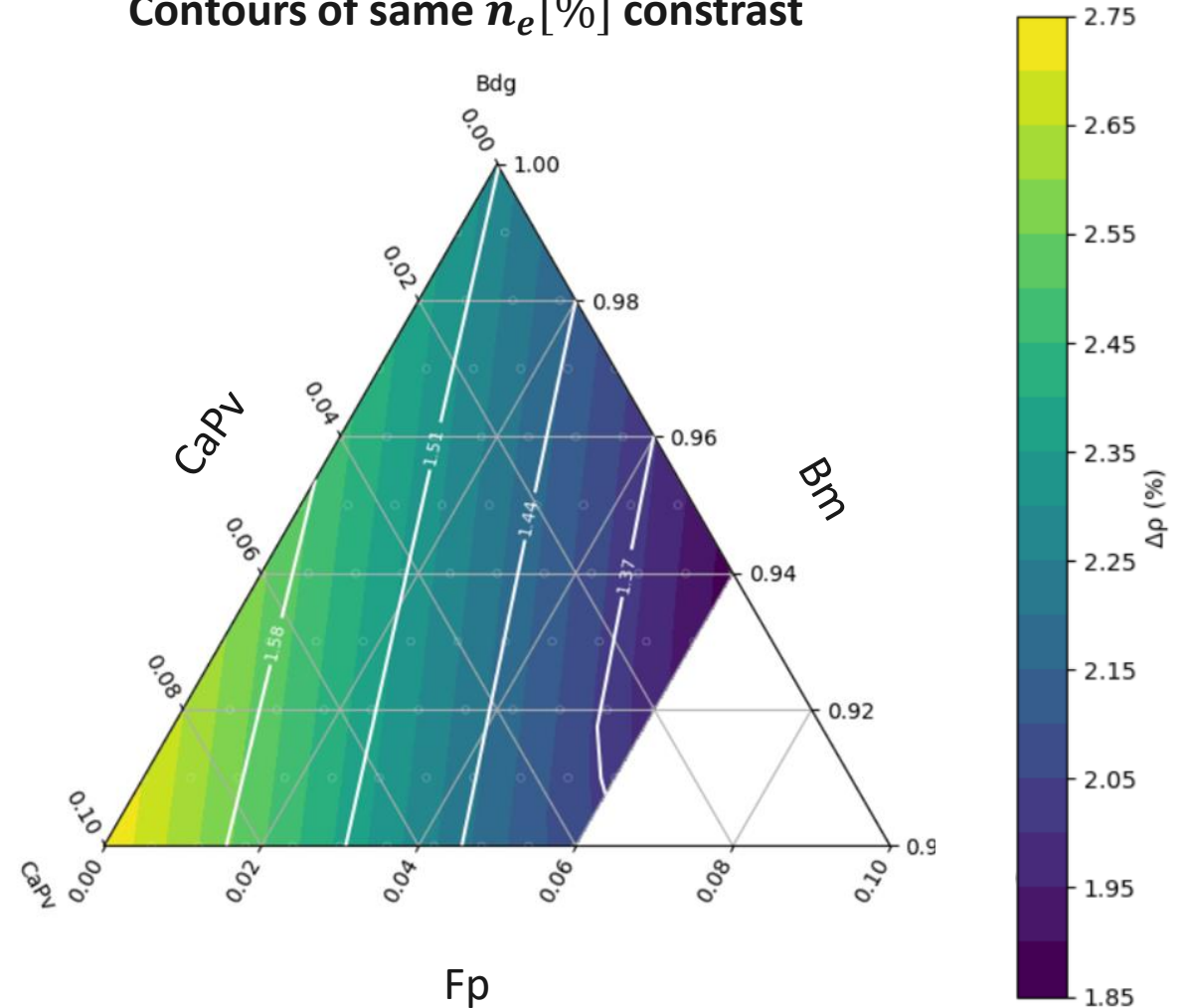


Using Vilella et al.'s end-member composition, we choose assemblages that meet the stated bulk conditions

Contours of same V_s [%] anomaly



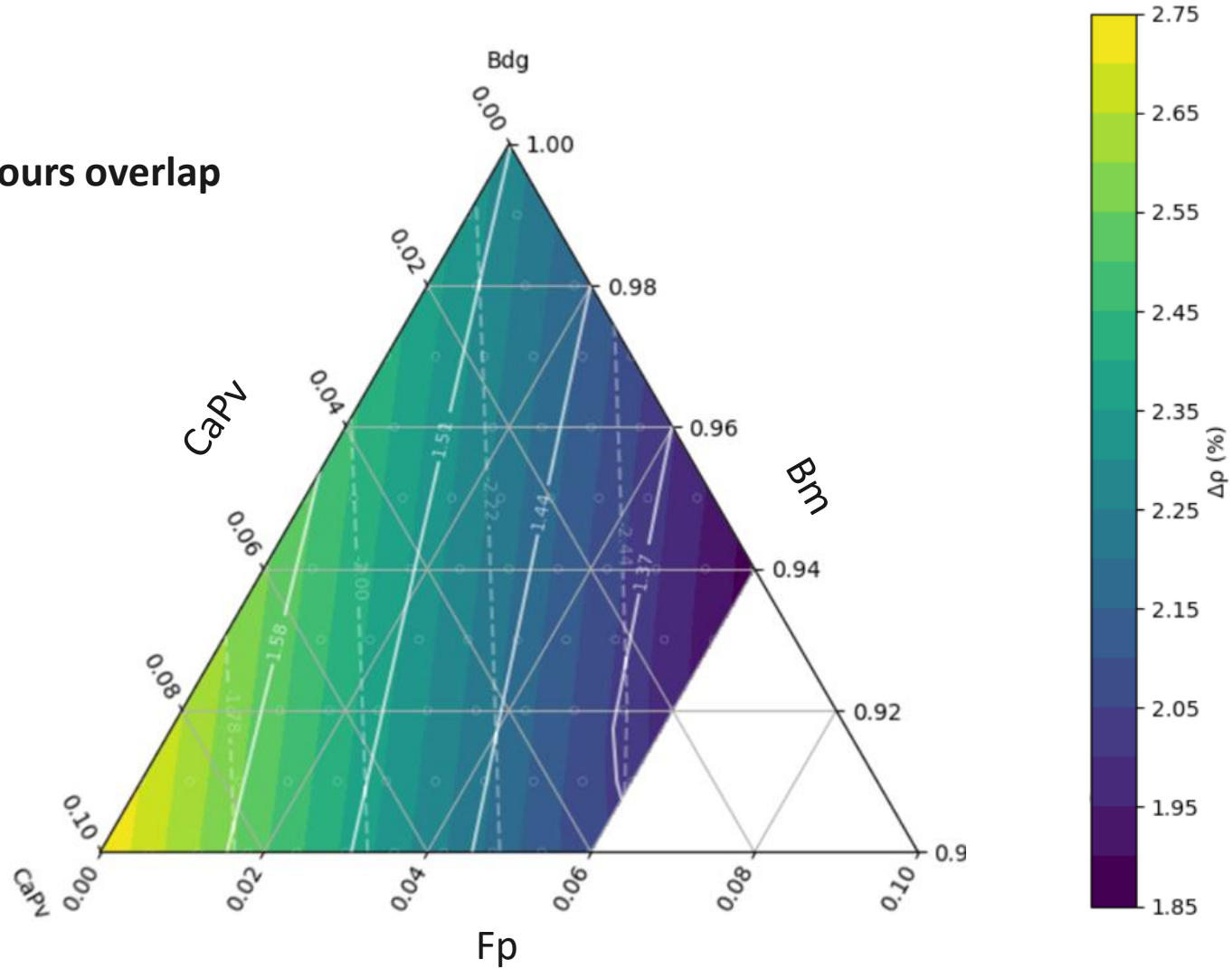
Contours of same n_e [%] constraint





Using Vilella et al.'s end-member composition, we choose assemblages that meet the stated bulk conditions

Contours overlap

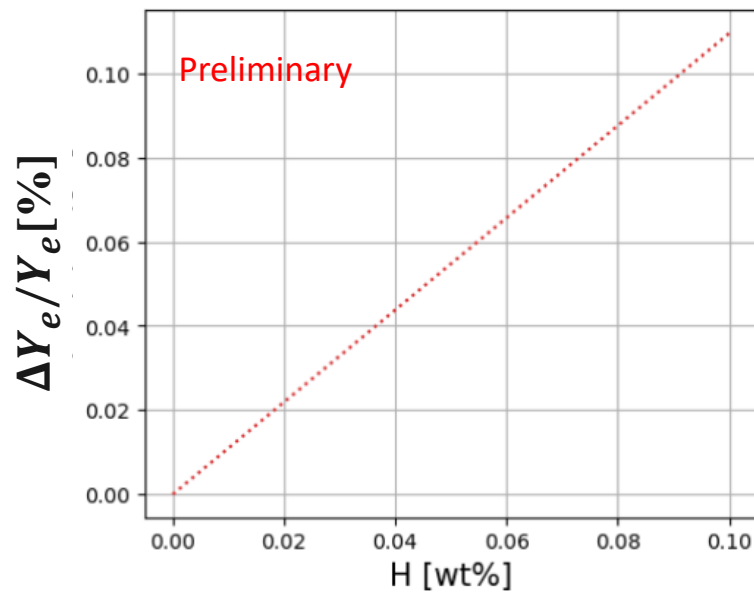




Hydrogen can be stored in Bridgmanite and in CaPv, if present Y_e and ρ might show significant contrast

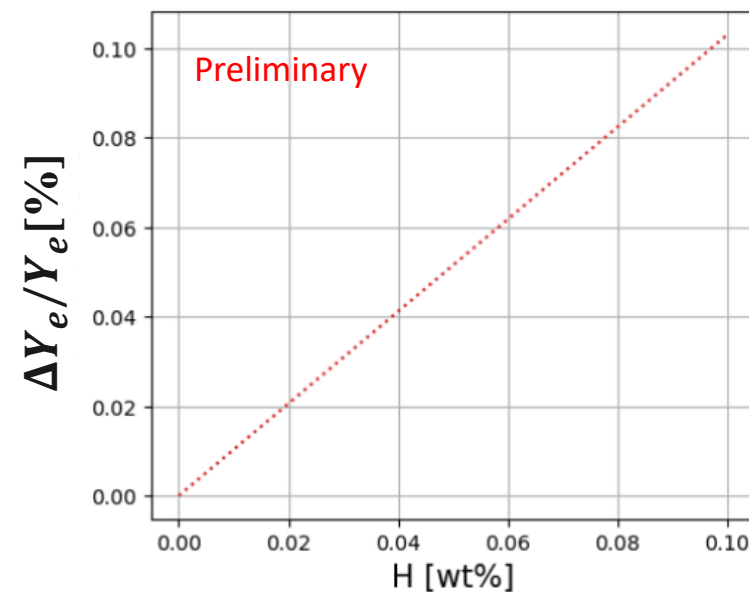
Mechanism: $Mg_{1-x}H_{2x}SiO_3$

Estimated storage capacity up to 0.1 wt%



Mechanism: $Ca_{1-x}H_{2x}SiO_3$

Estimated storage capacity up to 0.2 wt%





Hydrogen can be stored in MgSiO₃ and in CaPv, if present Y_e and ρ might show stronger contrast

Hydrous Bm: $Mg_{1-x}H_{2x}SiO_3$

Estimated storage capacity up to 0.1

JGR Solid Earth

RESEARCH ARTICLE

10.1029/2024JB030403

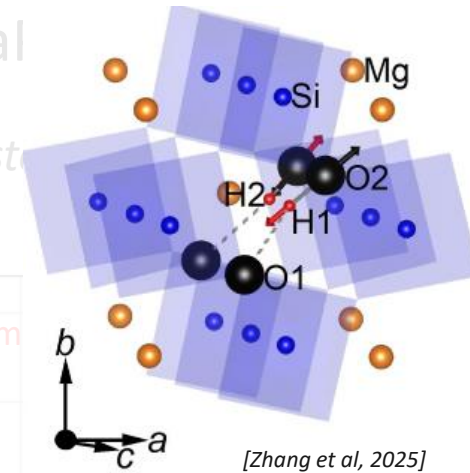
Accepted 8 JAN 2025

Hydrogen Dissolution Mechanisms in Bridgmanite by First-Principles Calculations and Infrared Spectroscopy

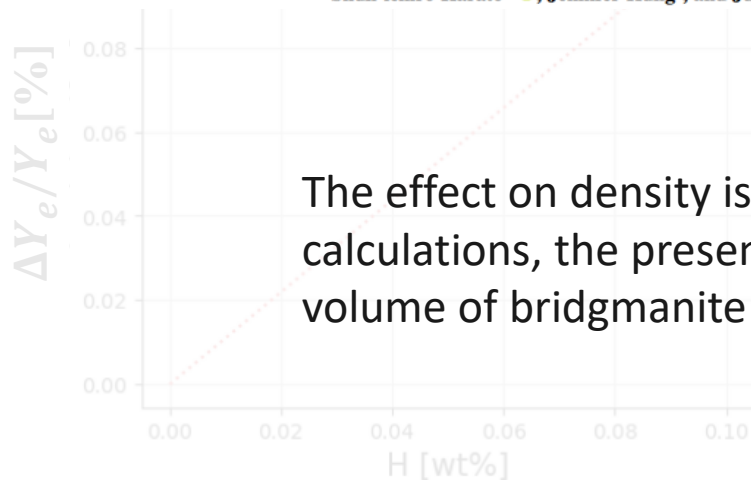
Yanyao Zhang^{1,2}, Jun Tsuchiya³, ChingChien Li⁴, Zefang Ye⁵, Wei Yan⁶, Takuo Okuchi⁷, Shun-ichiro Karato⁸, Jennifer Kung⁴, and Jung-Fu Lin¹

Hydrous Cal

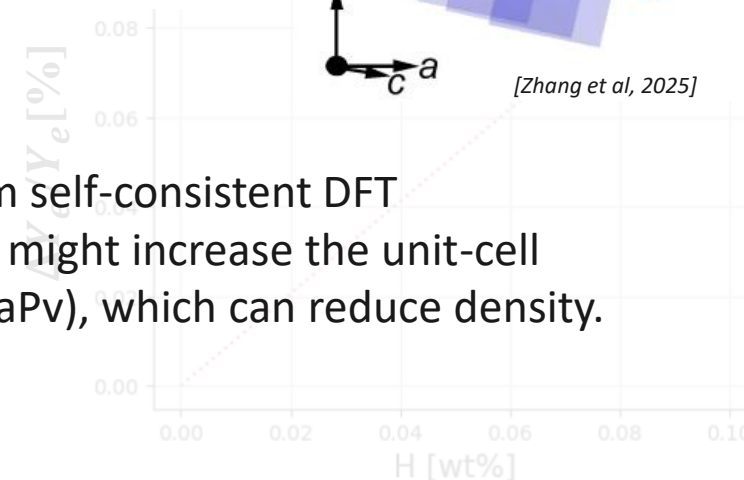
Estimated st



Hydrous
Bridgmanite
cell cluster



The effect on density is not trivial. From self-consistent DFT calculations, the presence of hydrogen might increase the unit-cell volume of bridgmanite (and possibly CaPv), which can reduce density.





Concluding remarks

- **There is a theoretical LLVP signal. The job now is to increase sensitivity by:**
 1. Pushing the detector performance as close as possible to the ideal case
 2. Increasing exposure, ε_{exp} , since $\Delta\chi_{\sigma}^2 = \varepsilon_{exp}\Delta\chi^2 \rightarrow$ My proposal: multi-detector configuration
- **Electron number density could serve as a new independent constraint for deep Earth geophysics**

Ongoing and Future Work

- Improving sensitivity: exploring a multi-detector approach
- Incorporating the effect of hydrogen in LLVP minerals



Thank you

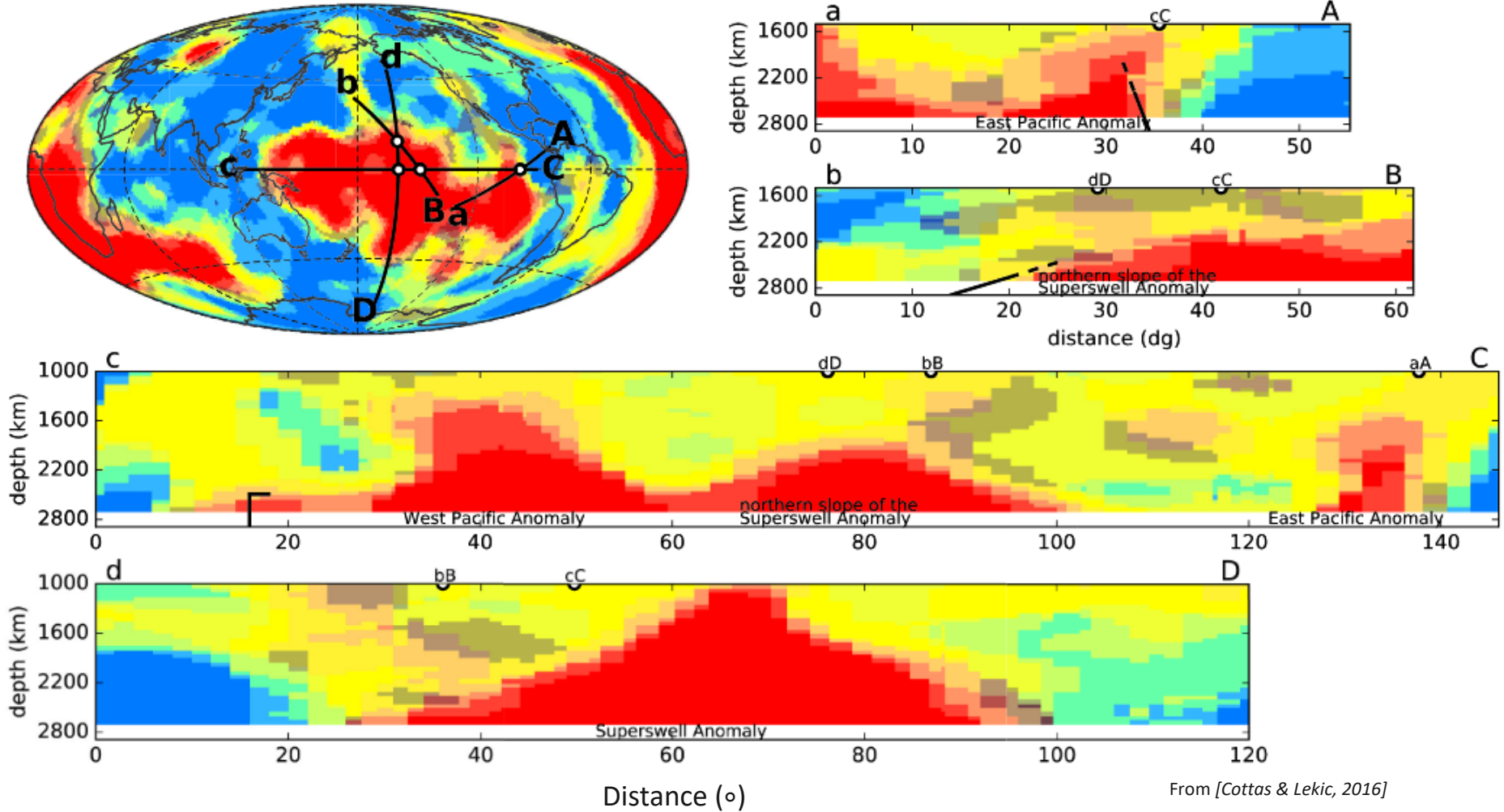


The Neutrino Tomography team



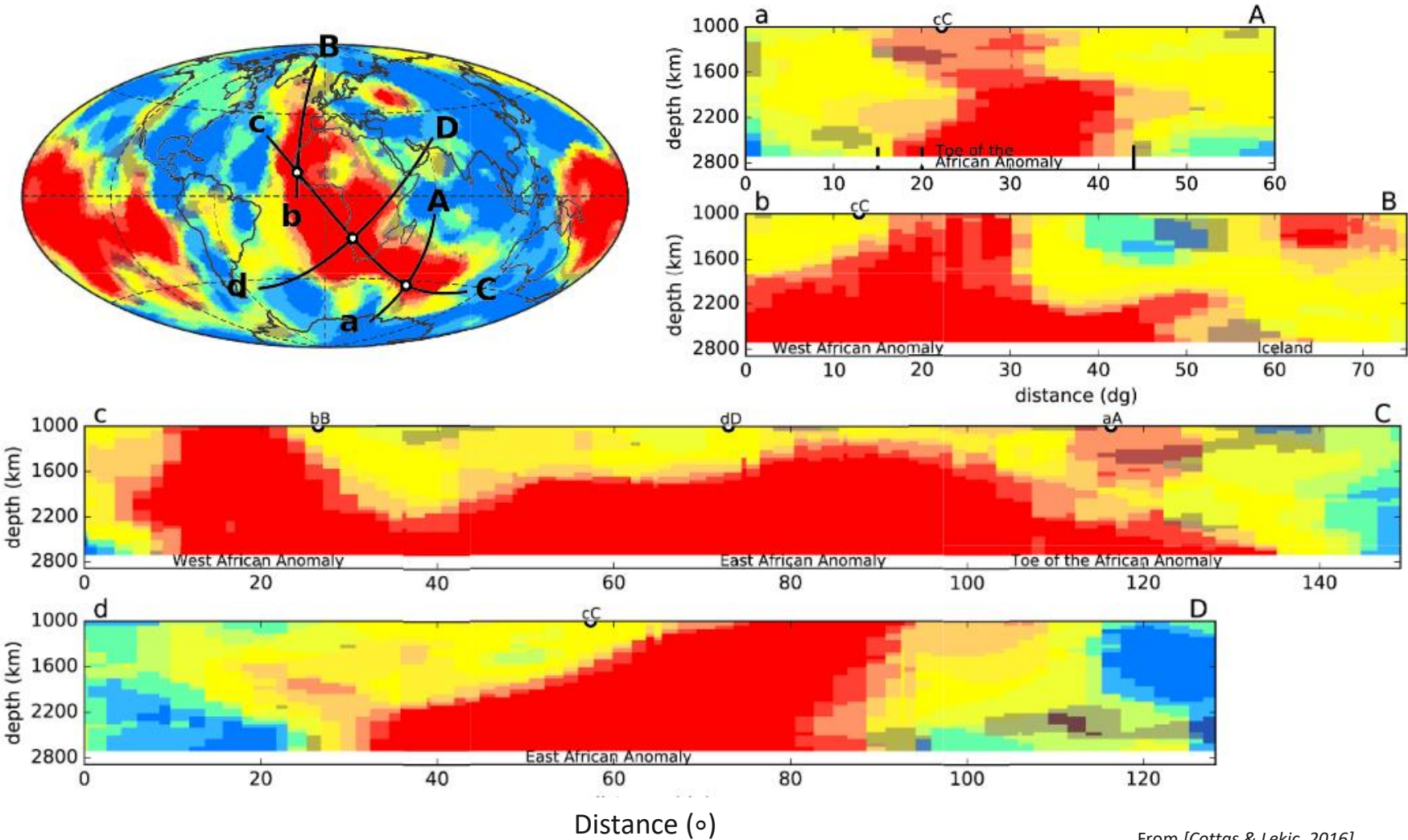
Supplementary Slides

LLVP dimensions (Pacific)



From [Cottas & Lekic, 2016]

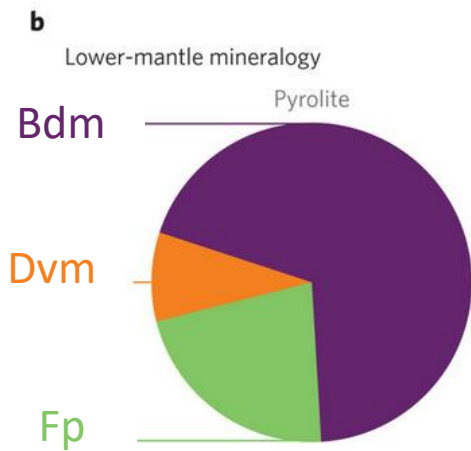
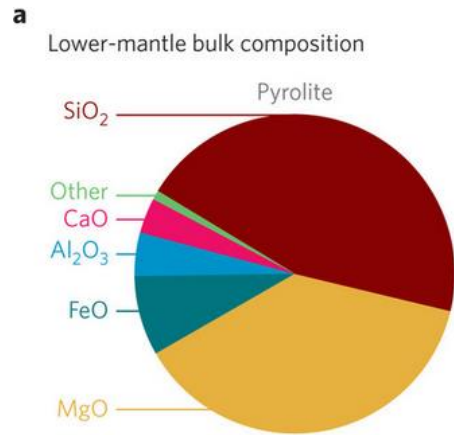
LLVP dimensions (African)



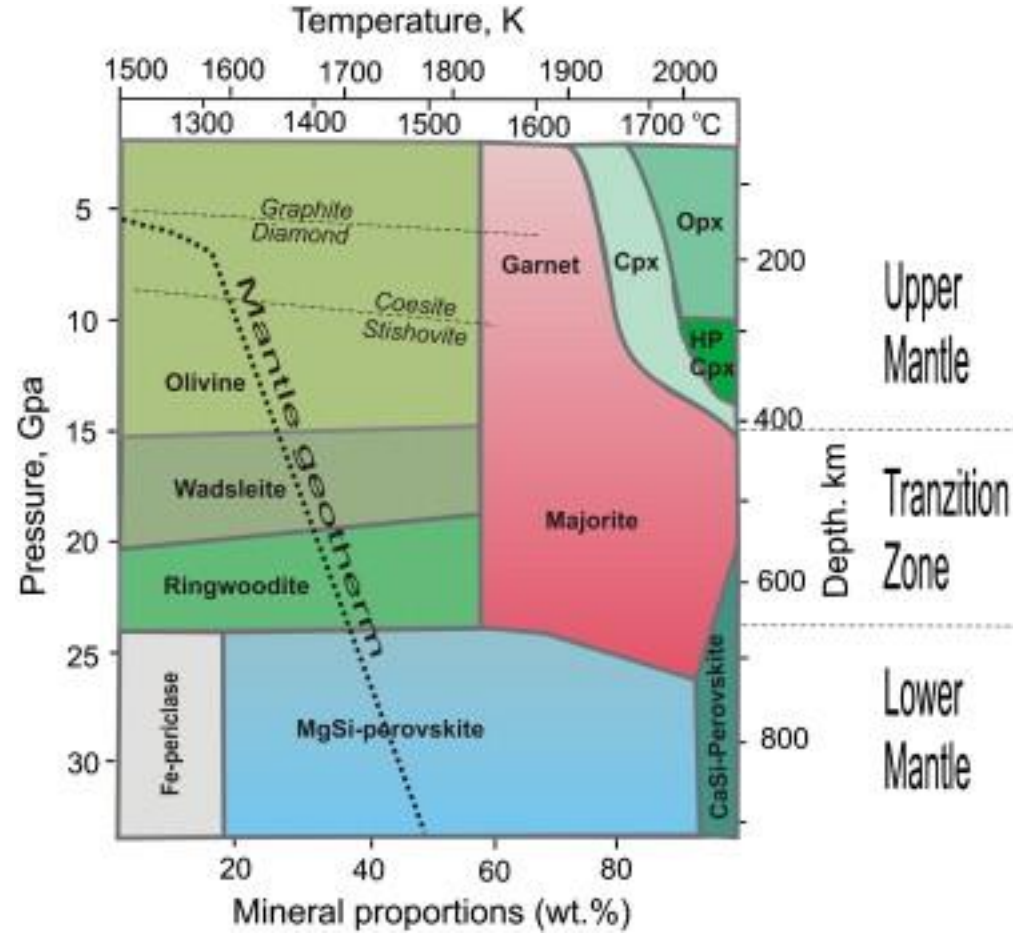
From [Cottas & Lekic, 2016]



Lower mantle mineralogy



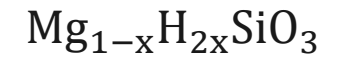
From [Garnero, 2016]



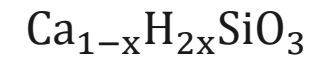
From [Kamisky, 2012]

Cation vacancy mechanisms:

Brigmanite ($MgSiO_3$ -perovskite)



Davemantite ($CaSiO_3$ -perovskite)





Detector Parametrization

Detector	M (Mton)	E_{th} (GeV)	E_{pl} (GeV)	$\sigma(E)/E$	σ_{θ} (deg)	E_{th}^{class} (GeV)	E_{pl}^{class} (GeV)	P_{max}^{class}
ORCA-like	8	2	10	25%	$30/\sqrt{E}$	2	10	85%
Hyper-Kamiokande-like	0.40	0.1	0.2	15%	$15/\sqrt{E}$	0.1	0.2	99%
DUNE-like	0.04	0.1	0.2	5%	5	0.1	0.2	99%
Next-Generation	10	0.5	1.0	$5\% + 10\%/\sqrt{E}$	$2 + 10/\sqrt{E}$	0.5	1	99%

Taken from [Maderer et al; 2023]

Angular resolution parametrization
(Von-Mises Fisher)

$$\frac{\kappa}{4\pi \sinh \kappa} e^{\kappa \cdot x(\theta_z^{int}, \phi^{int})^T \mu(\theta_z^{reco}, \phi^{reco})} \sin \theta_z^{int}$$

Concentration parameter κ :

$$\kappa(E^{int}) = \left(\frac{1}{\sigma_E(E^{int})} \right)^2$$

Energy resolution parametrization
(Gaussian)

$$\frac{1}{\sqrt{2\pi}\sigma_E(E^{int})} \cdot e^{-\frac{1}{2} \frac{(E^{int} - E^{reco})^2}{\sigma_E^2(E^{int})}}$$

Next-Gen detector:

$$\sigma_E(E^{int})/E^{int} = 5\% + 10\%/\sqrt{E^{int}}$$

$$\sigma_{\theta} = 2^{\circ} + 10^{\circ}/\sqrt{E^{int}}$$

Event Calculation and binning scheme

Interacting rates

$$R_{\nu\alpha}^{int}(E_{\nu,i}^{int}, \theta_{Z,j}^{int}, \phi_k^{int}) = \sum_{\beta=e,\mu} \left(\frac{\sigma_{\nu\alpha}^{CC}(E_{\nu,i}^{int})}{m_N} \cdot \frac{d^4\Phi^{\nu\beta}}{dE_\nu d\theta_Z d\phi dt}(E_{\nu,i}^{int}, \theta_{Z,j}^{int}, \phi_k^{int}) \cdot P_{\beta\alpha}^m(E_{\nu,i}^{int}, \theta_{Z,j}^{int}, \phi_k^{int}) + \frac{\sigma_{\bar{\nu}\alpha}^{CC}(E_{\nu,i}^{int})}{m_N} \cdot \frac{d^4\Phi^{\bar{\nu}\beta}}{dE_\nu d\theta_Z d\phi dt}(E_{\nu,i}^{int}, \theta_{Z,j}^{int}, \phi_k^{int}) \cdot P_{\beta\bar{\alpha}}^m(E_{\nu,i}^{int}, \theta_{Z,j}^{int}, \phi_k^{int}) \right)$$

Reconstructed rates

$$R_{\nu\alpha}^{reco}(E_{\nu,m}^{reco}, \theta_{Z,n}^{reco}, \phi_l^{reco}) = \sum_{i,j,l} \left(PDF_{\vec{x}}(\theta_{Z,n}^{reco}, \phi_l^{reco}; \theta_{Z,j}^{int}, \phi_k^{int}, \kappa(E_{\nu,i}^{int})) \times PDF_{E_\nu}(E_{\nu,m}^{reco}; E_{\nu,i}^{int}) \times R_{\nu\alpha}^{int}(E_{\nu,i}^{int}, \theta_{Z,j}^{int}, \phi_k^{int}) \times (\Delta E_{\nu,i}^{int} \cdot \Delta \theta_{Z,j}^{int} \cdot \Delta \phi_k^{int}) \right)$$

Adaptative binning in energy

$$E_{\nu;l,mid}^{reco} = E_{\nu;l,low}^{reco} + \frac{1}{2}\sigma_E(E_{\nu;l,mid}^{reco})$$

$$E_{\nu;l,up}^{reco} = E_{\nu;l,mid}^{reco} + \frac{1}{2}\sigma_E(E_{\nu;l,mid}^{reco})$$

Log-likelihood test

For poisson distributed Neutrino dataset $\vec{N} = \{n_{ijk(lmn)}\}$

$$LLR(\vec{N}_{obs}^{int(reco)}, \vec{N}_{exp}^{int(reco)}) = -2 \cdot \ln \left(\frac{L(\vec{N}_{exp}^{int(reco)}, \vec{N}_{exp}^{int(reco)})}{L(\vec{N}_{obs}^{int(reco)}, \vec{N}_{exp}^{int(reco)})} \right)$$

$$LLR(\vec{N}_{obs}^{int(reco)}, \vec{N}_{exp}^{int(reco)}) = 2 \sum_{i,j,k(m,n,l)} \left(n_{obs;ijk(mnl)}^{int(reco)} - n_{obs;ijk(mnl)}^{int(reco)} \right) + n_{obs;ijk(mnl)}^{int(reco)} \cdot \ln \left(\frac{n_{obs;ijk(mnl)}^{int(reco)}}{n_{obs;ijk(mnl)}^{int(reco)}} \right)$$

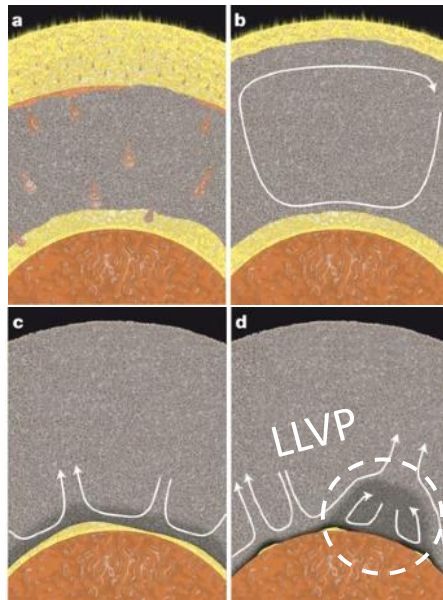
Hypothesis

$$H_0 = \vec{N}_{Exp} \sim \vec{N}_{Obs} \text{ (No difference in dataset)}$$

$$H = \vec{N}_{Exp} \neq \vec{N}_{Obs} \text{ (Dataset is different)}$$

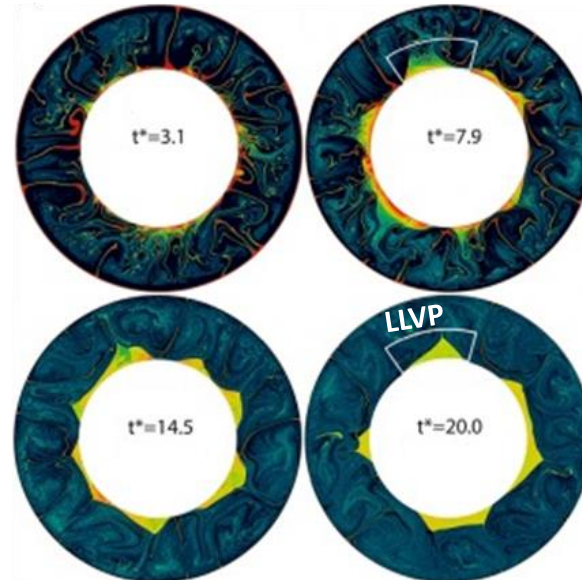
Multiple candidate pathways may accumulate the compositionally distinct material thought to form thermochemical LLVPs

Primordial material



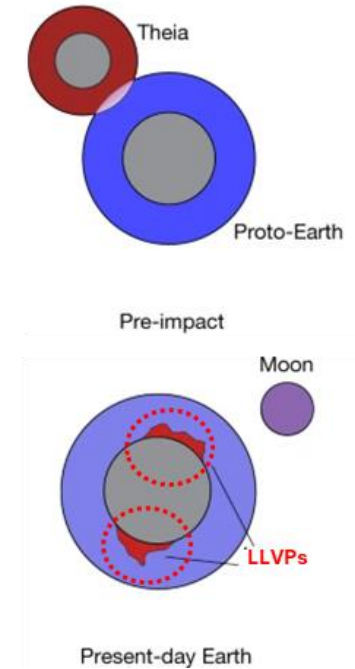
Modified from [Labrosse et al 2007]

Subducted oceanic crust



Modified from [Li & McNamara, 2022]

Remnant of a Proto Planet (Theia) Material



Modified from [Yuan et al, 2023]